The Astrophysical Journal, 888:69 (15pp), 2020 January 10 https://doi.org/10.3847/1538-4357/ab5f0d

Analytic Model for the Time-dependent Electromagnetic Field of an Astrophysical Jet

P. M. Bellan
Applied Physics and Materials Science, Caltech, Pasadena, CA 91125, USA; pbellan@caltech.edu
Received 2019 May 20; revised 2019 November 17; accepted 2019 December 3; published 2020 January 9

Abstract

An analytic model of the time-dependent electric and magnetic fields of an astrophysical jet is presented. These fields satisfy the time-dependent Faraday's law and describe a jet with increasing length. The electric field contains both electrostatic and inductive parts. The electrostatic part corresponds to the rate of injection of toroidal magnetic flux, while the sum of the electrostatic and inductive parts results in the electric field parallel to the magnetic field being zero everywhere. The pinch force associated with the electric current provides a peaked pressure on the jet axis and a pressure minimum at the radius where the poloidal magnetic field reverses direction.

Unified Astronomy Thesaurus concepts: Accretion (14); Jets (870); Magnetohydrodynamics (1964); Stellar jets (1607); Stellar accretion disks (1579); Young stellar objects (1834); Collimation (268)

1. Introduction

Astrophysical jets were first observed over a century ago by Curtis (1918), but their magnetic character was only realized more recently; a review of recent observational, theoretical, and computational advances is given in Pudritz & Ray (2019). The essential observed features of astrophysical jets are axisymmetry, association with an accretion disk (presumed to be the energy source), bidirectionality, collimation, and a finite length that it is increasing with time.

Astrophysical jets have been studied via observation of actual jets, analytic modeling, numerical modeling, and simulation by laboratory experiments. Each of these approaches has advantages and disadvantages. Actual observation proves the existence of jets and reveals features that need to be explained but suffers from the shortcoming that many critical internal parameters such as density, electric current, and magnetic field of the jet cannot be resolved or quantified. Analytic models provide an understanding of interrelationships between fundamental parameters but can mischaracterize critical aspects such as time dependence, finite dimensions, boundary conditions, and length increasing with time. Simulation by laboratory experiments can provide insights into many relevant aspects and, in principle, experiments can be fully diagnosed, but questions can be raised whether an experiment is a true scale model of actual astrophysical jets and whether relevant parameter regimes are being addressed.

Several ways to categorize astrophysical jets have been proposed, including, but probably not limited to, the following: jets can be relativistic or nonrelativistic; the jet energy flux can be predominantly from the Poynting flux or from particle kinetic energy (hydrodynamic), or these two types of flux could be comparable; jets could be launched by magnetic forces, by hydrodynamic pressure gradients, or by centrifugal effects; and jets could emanate from young stellar objects (YSOs or newborn stars), or they could emanate from black holes or active galactic nuclei (AGNs). The size of jets could be of the order of the solar system, or they could be much larger. From an observational point of view, relativistic jets are associated with black holes or AGNs and are very large (kiloparsecs to megaparsecs), while nonrelativistic jets are associated with YSOs and have dimensions of the order of the solar system (10^{-3} pc).

Astrophysical jets were first modeled analytically with important models presented by Mestel (1961), Blandford & Payne (1982), Lynden-Bell (2003), and Pudritz et al. (2012). A review of analytic models has been provided by Beskin (2010). In order to be tractable, the analytic models typically assumed that the magnetic field is stationary, self-similar, and force-free.

The Blandford and Payne analytic model provided a physical picture where it was assumed that plasma flows along the magnetic field like beads on a wire, as proposed by Henriksen & Rayburn (1971). The consequence is that in a helical magnetic field, the plasma flow would have an angular velocity component with associated centrifugal force. The next step in this argument was to assume that the helix radius increases with axial displacement so that the centrifugal force would drive the plasma to larger radius and so, because of the flaring, to a larger axial position. This beads-on-a-wire concept has been used by many authors, for example Livio (1999) and Dal Pino (2005).

Because of advances in computational power, it has become possible to solve the time-dependent magnetohydrodynamic (MHD) equations numerically and so obtain numerical models that are time dependent, not self-similar, and not force-free (Shibata & Uchida 1986; Stone & Norman 1992; Pudritz et al. 2012; Nakamura et al. 2010; Zhai et al. 2014). The MHD simulations can also model deviations from axisymmetry such as kink instabilities. While more realistic than the earlier analytic models, the numerical MHD solutions also have shortcomings. In particular, the electric field $\boldsymbol{E}(\boldsymbol{x},t)$ is not explicitly determined because $\boldsymbol{E}(\boldsymbol{x},t)$ is eliminated from the system of equations when Faraday's law and Ohm's law are combined to produce the induction equation. This elimination of the electric field makes it difficult to calculate test particle trajectories, so it is unclear how the sum of individual particle motions results in the net fluid behavior. A second problem involves the boundary condition at the jet origin. The lengthening jet necessarily involves an increase of toroidal magnetic flux, but ideal MHD does not allow for the flux linked by a given amount of plasma to change. Essentially there has to be some kind of "battery" that imposes a voltage drop across the plasma; this voltage drop represents the rate of flux injection. The ideal MHD equations do not allow insertion of a battery into the plasma, so some sort of non-MHD boundary condition must be applied, as was done in Zhai et al. (2014).

Astrophysical jets have been simulated in laboratory experiments using pulsed power technology by Hsu & Bellan (2002),

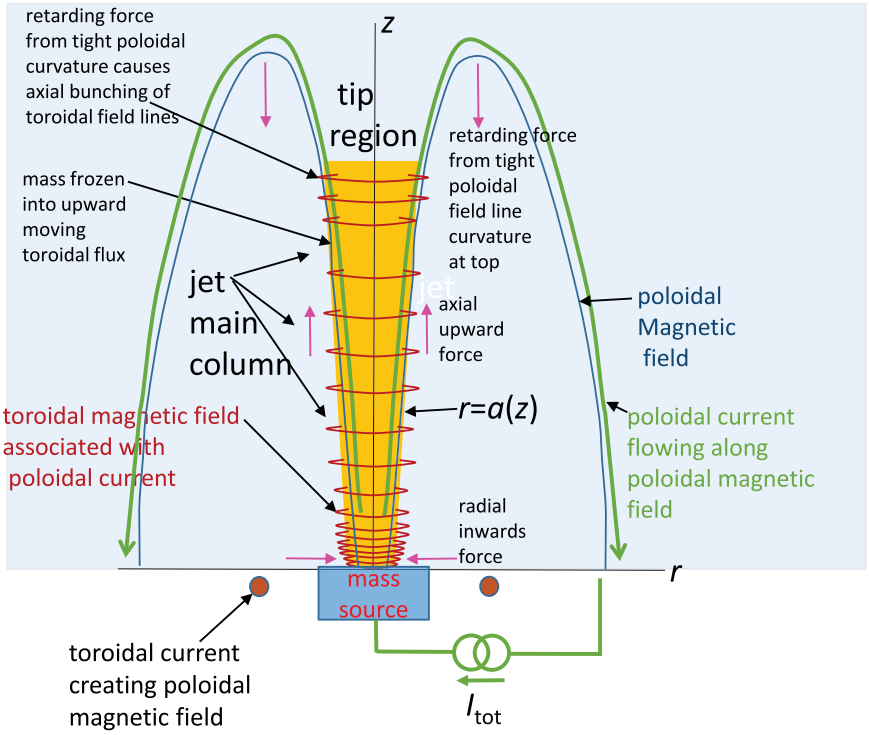

Figure 1. Sketch showing jet topology. (Reproduced from Bellan (2018a) with the permission of AIP Publishing.)

Lebedev et al. (2005), You et al. (2005), Gourdain & Seyler (2014), and Lavine & You (2019). Experiments simulating astrophysical jets using pulsed power have been reviewed by Lebedev et al. (2019), and experimental observations have been reproduced using 3D MHD numerical codes by Ciardi et al. (2007), Huarte-Espinosa et al. (2013), and Zhai et al. (2014). Li et al. (2016) have simulated astrophysical jets in a laboratory experiment that used a high-power laser. Ryutov et al. (2001) presented criteria for scaling laboratory experiments to astrophysical situations.

The author recently presented analytic models that allow for time-dependent magnetic fields, increasing length, and the means for imposing the appropriate non-MHD boundary conditions at the accretion disk (see Bellan 2008, 2017, 2018a, 2018c). Jet topology is sketched in Figure 1. This topology is motivated by laboratory experiments such as shown in Figure 2 and by 3D numerical MHD simulations of jets such as those by Ouyed & Pudritz (1997), Kato (2007), and Zhai et al. (2014). The $z = 0$ plane corresponds to the accretion disk. This plane provides the mass source, shown as the blue box in Figure 1, for the jet. This plane also contains the electrical power supply that drives the poloidal current that creates the toroidal magnetic field.

The discussion in Bellan (2018a) shows that the magnetic force can be decomposed into two terms, each orthogonal to the magnetic field. Thus the magnetic force is $\boldsymbol{J}\times\boldsymbol{B} = -B^2\hat{\boldsymbol{R}}/(R\mu_0) - \nabla_\perp B^2/(2\mu_0)$ (see also p. 72 in Kulsrud 2005). The $-B^2\hat{\boldsymbol{R}}/(R\mu_0)$ term is denoted as the curvature force and is directed toward the center of curvature of a curved magnetic field having a local radius of curvature vector $\boldsymbol{R}$, while the $-\nabla_\perp B^2/(2\mu_0)$ term is denoted as the magnetic pressure term and behaves as a pressure that pushes from regions of high B^2 to regions of low B^2 but only in the direction perpendicular to $\boldsymbol{B}$. The curvature force and the magnetic pressure force are not in general orthogonal to each other, and in the specific case of a vacuum or potential field (i.e., field for which $\boldsymbol{J} = 0$), these two forces cancel each other exactly.

The curvature force acts to decrease the radius of the red circles in Figure 1. The curvature force also provides a retarding force associated with the curvature of the green poloidal field line in Figure 1. The pressure force provides an axially upward force at the lower jet region in Figure 1 where the density of the red circles is large. This upward force is proportional to the density of red circles (i.e., to $-\partial B_\phi^2/\partial z$). The jet main column is nearly collimated and has nearly constant velocity. The jet tip region has a partial deceleration as a result of the retarding force from the curvature of the poloidal magnetic field in this region. The jet mass, shown as orange, is frozen to both the poloidal and toroidal magnetic flux. The toroidal magnetic flux is given by the density of the red circles, so this freezing corresponds to the red circles moving with the jet flow. The radial pinching of the red circles results in a high hydrodynamic pressure on the jet axis. Since the number of red circles increases with time as the jet lengthens, the toroidal flux linked by the disk is increasing, and the rate of increase of this flux is manifested by a voltage appearing across the power supply. This is indicated by the two overlapping green circles that are driving the current I_{tot} that flows in the poloidal direction and creates the toroidal magnetic field (red circles). Sequences of images of laboratory jets consistent with this discussion are shown in Figure 2. A 3D numerical MHD astrophysical jet code used by Zhai et al. (2014) to model this experiment produced poloidal magnetic fields, toroidal magnetic fields, and collimated jets consistent with this picture. As shown in Figure 5 of Zhai et al. (2014), synthetic jet image sequences created in the code are essentially identical to sequences of camera images of the laboratory jet.

The models in Bellan (2008, 2017, 2018a, 2018c) are in the context of MHD and so do not provide a complete description of the electric fields or of particle motion. These models

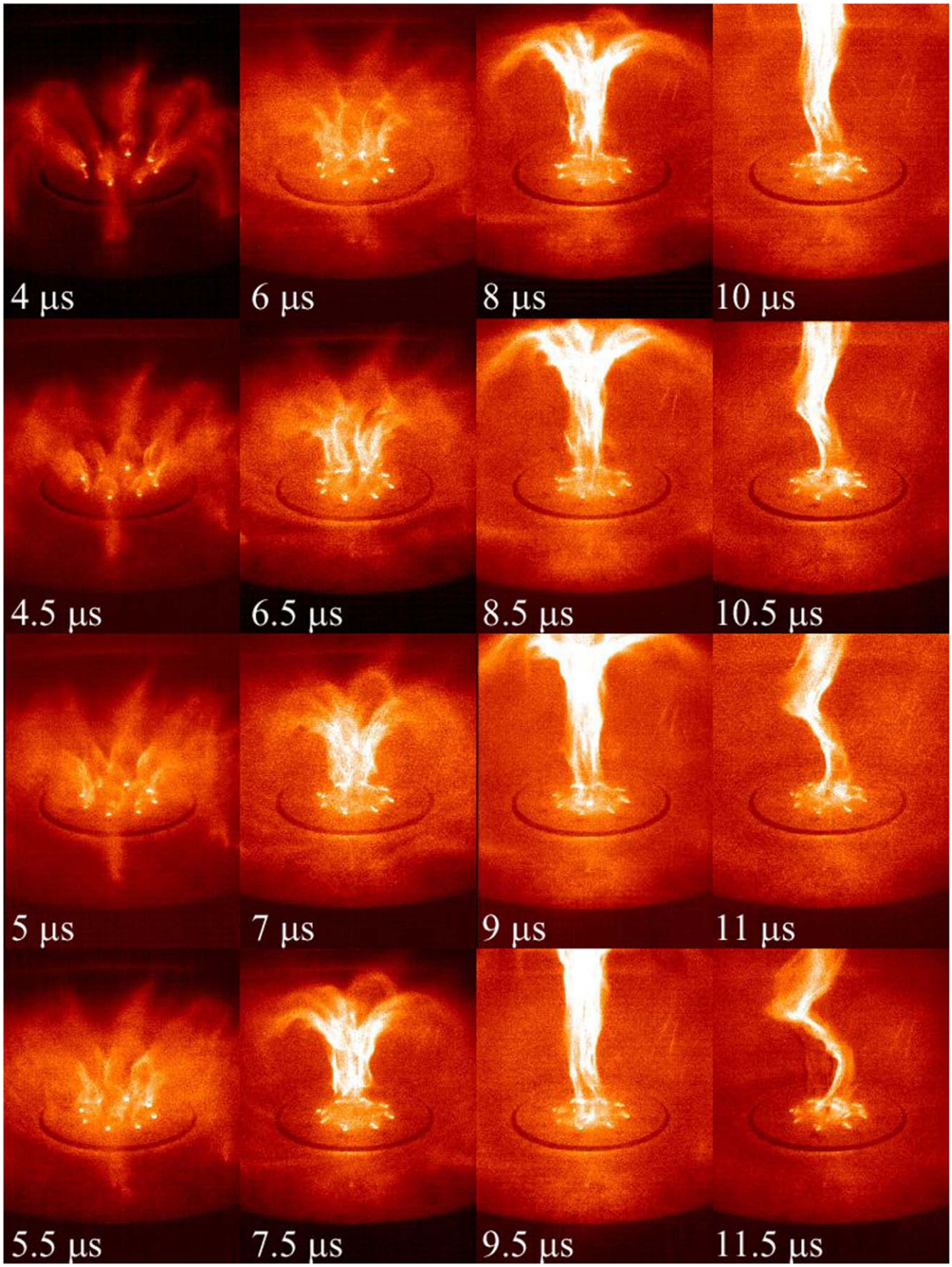

Figure 2. Development of collimated jet in a Caltech lab experiment (figure reprinted with permission from You et al. (2005), © 2005 by the American Physical Society).

subdivided the jet into launching region, main body, and tip, as shown in Figure 1 with a detailed discussion of each region, but there was only a qualitative linking of these three regions to each other. The main conclusions of these models were the requirements for a radial voltage drop, mass injection, an electric power source at the launching region, and that the jet collimation was a consequence of the axial force, velocity, and acceleration all depending on axial position. These models combine the properties that (1) magnetic flux is frozen into the frame of a moving plasma and (2) the $\boldsymbol{J} \times \boldsymbol{B}$ magnetic force can be decomposed into curvature and pressure gradient terms.

The purpose of this paper is to present a model that addresses some of the shortcomings of the previous analytic models. Although imperfect and a simplification like all models, this new model is nevertheless useful because it provides a complementary point of view that clarifies important issues missing from previous models. Furthermore, identification of the model's weaknesses points to new questions for which future answers will provide additional insights. The model is based in part on a method used by Harris (1962) to characterize the basic Z-pinch first described by Bennett (1934). The model presented here is nonrelativistic and therefore is relevant to nonrelativistic jets associated with YSOs and to laboratory experiments. It likely could be extended to relativistic situations, but this would add a layer of complexity that would obscure understanding at this stage of development since the basic ideas can be expressed in the much simpler nonrelativistic context. The model is relevant to jets where Poynting flux dominates or where Poynting flux is comparable to hydromagnetic flux; for reasons discussed below, the model does not propose that centrifugal effects drive jets.

The key idea is to use Lorentz transformations to switch between the lab frame where the situation is time dependent and a virtual frame where the situation is static. These transformations are done in the nonrelativistic limit, but could be extended to relativistic situations. The essential feature is that the Lorentz transformation provides the correct time dependence, where "correct" means that the time-dependent Faraday's law is satisfied in the lab frame. This important feature was missing from the earlier analytic models of Mestel (1961), Blandford & Payne (1982), Sauty (1994), Lynden-Bell (2003), Beskin (2010), and Pudritz et al. (2012). These previous analytic models assumed the magnetic field was static, an assumption that is incompatible with a magnetized jet having its length increase with time. The model presented here has a magnetic field that is time dependent in the lab frame, and this time dependence results in an associated electric field having both inductive and electrostatic components. However, unlike the lab-frame magnetic field, the virtual-frame magnetic field is time independent and has no associated electric field. A moderately complex static structure is first defined in the virtual frame. Transformation of this structure to the lab frame provides further and desired complexity while satisfying the time-dependent Faraday's law. The construction is arranged so that the lab-frame electric and magnetic fields have the morphology of a moving astrophysical jet, satisfy Ampere's and Faraday's laws, and, by satisfying $\boldsymbol{E} \cdot \boldsymbol{B} = 0$, are consistent with both ideal and Hall MHD. The electrostatic part of the lab-frame electric field corresponds to the rate of toroidal flux injection associated with the continuous increase of the jet length and hence increase in toroidal flux. One significant consequence of this time-dependent solution is that it clearly shows that the plasma does not move like a bead on a wire but instead has a strict axial motion despite the magnetic field being helical.

The analytic functions produce a twisted magnetic field having the topology of a propagating astrophysical jet. However, the model is an oversimplification because a constant, uniform jet velocity is assumed. Thus the model fails to describe the internal accelerations, decelerations, and velocity shear as would be determined by a numerical solution of the MHD equations. Thus, the model incorporates the topology depicted in Figure 1 but does not follow the subtleties resulting from there being gradients in the density of the red circles or a retarding force from the curvature of the green poloidal field lines. The model effectively still has the red circles moving with the flow, so the number of red circles and hence the toroidal flux increase as the jet becomes longer, but it does not attempt to describe how the variation of the density of the red circles drives the axial flow. The axial flow is simply assumed to exist. However, while the model does not attempt to depict the axial forces and their consequences, it does depict the radial forces and their consequence, namely the high pressure on the jet axis as a result of the red circles trying to reduce their radius of curvature (i.e., the pinch force).

The omission of a detailed characterization of the axial forces means that axial acceleration is not depicted, but this does not seriously detract from insights regarding electric and magnetic field evolution because these depend on the jet position and velocity but not on the jet acceleration. The virtue of the model is that because the electromagnetic fields are specified by analytic functions, it becomes possible to calculate moderately realistic particle trajectories. Thus, the model provides insights missing from numerical MHD models and from previous analytic models. Being time independent, the earlier analytic models had no inductive electric field, no time-changing magnetic field, and no possibility for the jet length to increase. Many of the previous analytic models assumed self-similarity and so could not identify the different roles played by the different regions shown in Figure 1. The assumption of self-similarity means that it is assumed that all parts of the jet behave the same way and that the jet has no end.

2. Magnetic Field and Flux

Essential features of observed astrophysical jets are that they are (1) axisymmetric, (2) appear as narrow, relatively dense cylindrical structures with a starting point beginning at a fixed plane (accretion disk), (3) have a finite length that is increasing with time, and (4) contain poloidal and toroidal magnetic fields that are finite in extent and energy but have extent changing with time as the jet lengthens. The finite extent of the jets (i.e., having a beginning, a midregion, and an end) cannot be described by self-similar models. This indicates the need for a more complex model that incorporates distinct regions, namely beginning, midregion, and end. The lengthening of the jet with time indicates that jets cannot be described by static models since a static model cannot increase the jet length. Previous analytic models have assumed self-similarity and so did not have the capacity to characterize the different regions of the jet, the increasing length of the jet, or the time dependence of the fields (this will be discussed in detail in Section 9). While these shortcomings were acknowledged, it was presumed that they were not sufficiently serious to invalidate models. The analytic model we present here allows for characterizing the different

regions of the jet, the finiteness of the jet, the increasing length, and the time dependence of the fields. The discussion indicates that some of the simplifications made in previous analytic models are in fact serious and lead to misleading conclusions.

We now construct an axisymmetric analytic magnetic structure that has a narrow, relatively dense cylindrical structure with a fixed starting point, has a finite length that increases with time, contains poloidal and toroidal magnetic fields, and is consistent with magnetohydrodynamics in a semiquantitative fashion. By semiquantitative we mean that qualitative behaviors and relations are captured, but quantitative details may not be precise.

A cylindrical coordinate system $\{r,\ \phi,\ z\}$ will be used. Because of the assumed axisymmetry, the magnetic field can be expressed as

$$\boldsymbol{B} = \frac{1}{2\pi}\nabla\psi \times \nabla\phi + \frac{\mu_0 I}{2\pi}\nabla\phi, \tag{1}$$

where $\psi(r,\ z,\ t)$ is the poloidal flux, $I(r,\ z,\ t)$ is the poloidal current, and $\nabla\phi = \hat{\phi}/r$. The magnetic components then satisfy $2\pi r B_r = -\partial\psi/\partial z$, $2\pi r B_\phi = \mu_0 I$, and $2\pi r B_z = \partial\psi/\partial r$. The associated current density is determined from Ampere's law $\nabla \times \boldsymbol{B} = \mu_0 \boldsymbol{J}$ and is

$$\boldsymbol{J} = \frac{1}{2\pi}\nabla I \times \nabla\phi - \frac{r^2\nabla\phi}{2\pi\mu_0}\nabla\cdot\left(\frac{1}{r^2}\nabla\psi\right). \tag{2}$$

Since magnetic monopoles do not exist, the most basic magnetic source is a dipole. We thus use a dipole magnetic field as the elementary magnetic structure for constructing flux functions that provide the essential features of astrophysical jets. Unlike for monopoles, magnetic flux tubes emanating from a dipole do not go to infinity, but instead curve back and close upon themselves.

In order to lay the groundwork for the specification of the functional forms of $\psi(r,\ z,\ t)$ and $I(r,\ z,\ t)$ that characterize essential features of astrophysical jets, we begin by introducing as a reference the poloidal flux of a magnetic dipole located at $r = 0$, $z = -a/\sqrt{2}$. This static reference poloidal flux will be called the vacuum poloidal flux and is

$$\psi_{\rm vac}(r,\ z) = B_0\pi a^2\ \frac{r^2/a^2}{(2r^2/a^2 + (\sqrt{2}z/a + 1)^2)^{3/2}}. \tag{3}$$

The coefficients in Equation (3) have been chosen so that $B_z = B_0$ at $r = 0$, $z = 0$. The $z = 0$ plane can be thought of as the plane of an accretion disk. The magnetic dipole axial location is set to be at a negative position so that both the poloidal magnetic field and the poloidal magnetic flux are finite in the $z = 0$ plane and above.

An important feature of this specified flux function which will be shown below is that the associated $B_z = (2\pi r)^{-1}\,\partial\psi/\partial r$ reverses direction in the $z = 0$ plane at $r = a$. In this plane, B_z is positive for $0 < r < a$ and negative for $a < r < \infty$. Thus, the poloidal magnetic field has an umbrella-like topology. It is important to note that $\psi_{\rm vac}$ is a "vacuum" (also known as "potential") magnetic flux because $\psi_{\rm vac}$ has no associated toroidal current; that is, direct substitution of Equation (3) into the toroidal component of Equation (2) gives

$$J_{\phi,{\rm vac}} = -\frac{r}{2\pi\mu_0}\nabla\cdot\left(\frac{1}{r^2}\nabla\psi_{\rm vac}\right) = 0. \tag{4}$$

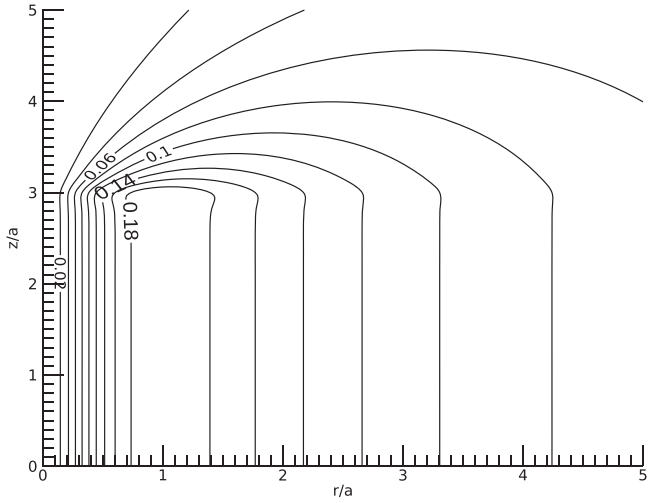

Figure 3. Flux contours $\psi(r,\ z,\ t)$ specified by Equation (5) for $v_0 t/a = 3$ and $\Delta/a = 0.1$.

Furthermore, because $\psi_{\rm vac}$ is time independent, it has no associated inductive electric field.

Although topologically similar to $\psi_{\rm vac}$, the jet poloidal flux ψ that will now be prescribed is not a vacuum flux because ψ has an associated toroidal current, that is, $\nabla\cdot(r^{-2}\nabla\psi) \neq 0$. The jet poloidal flux also differs from $\psi_{\rm vac}$ by being time dependent. The jet poloidal flux is prescribed as

$$\psi(r,\ z,\ t) = B_0\pi a^2\frac{r^2/a^2}{\left(\frac{2r^2}{a^2} + \left(\frac{\sqrt{2}}{a}G(z - v_0 t) + 1\right)^2\right)^{3/2}} \tag{5}$$

where v_0 is a constant velocity. The G function is prescribed to be

$$G(\xi) = \frac{\xi}{2} + \frac{\xi}{2}\tanh\left(\frac{\xi}{\Delta}\right) \tag{6}$$

where Δ is some short, fixed length. This G function acts as a z-stretching function and has been constructed so that (1) $G \to 0$ when ξ is large and negative and (2) $G \to \xi$ when ξ is large and positive. The form of the argument of G in Equation (5) will prove useful when performing Lorentz frame transformations.

The G function provides several useful limiting behaviors. If $t = 0$ and $z = 0$, then $z - v_0 t = 0$, so $G(z - v_0 t) = 0$, in which case

$$\psi(r,\ 0,\ 0) = B_0\pi a^2\frac{r^2/a^2}{(2r^2/a^2 + 1)^{3/2}}, \tag{7}$$

which is identical to $\psi_{\rm vac}$ in the $z = 0$ plane; this $\psi(r,\ 0,\ 0)$ flux profile will be denoted $\psi_{\rm disk}$. Thus, if the $z = 0$ plane corresponds to the symmetry plane of a bidirectional jet system, that is, to the midplane of an associated accretion disk, then $\psi(r,\ z,\ t) = \psi_{\rm vac}$ at $t = 0$ in the $z = 0$ plane. We now refer henceforth to the $z = 0$ plane as the disk plane. Figure 3 plots $\psi(r,\ z,\ t)$ as given by Equations (5) and (6) for the time when $v_0 t/a = 3$ and shows that the contours are stretched out in the z direction for $0 < z/a < 3$.

The poloidal flux function prescribed using Equations (5) and (6) is representative rather than unique in that it contains the essential features of a jet poloidal flux but does not preclude

the existence of other more complex functions that could also contain the essential features. An analogy would be to say that a sphere contains the essential features of a simply connected volume but does not preclude other shapes such as an ellipsoid also containing essential features of a simply connected volume.

The assumption of constant velocity is a simplification. In reality and as discussed in detail in Bellan (2018a), the velocity varies along the length of the jet such that there is acceleration at the base of the jet where the current density $\boldsymbol{J}$ and the magnetic field $\boldsymbol{B}$ are largest, so the $\boldsymbol{J}\times\boldsymbol{B}$ force accelerating the jet is the largest, there is a ballistic region for most of the jet length, and there is then a decelerating region just before the tip of the jet such that this deceleration results in collimation. The situation is somewhat analogous to traffic starting from rest at a red light on a highway, accelerating to a constant velocity, going a long distance at this constant velocity, and then slowing down when reaching a region of increased traffic density. Mass loading is relevant in the regions of acceleration and deceleration but not in the constant-velocity ballistic region. Thus, the simplifying assumption of constant velocity here effectively ignores the fact that increased mass loading reduces acceleration, but does not imply that the jet has zero mass or zero kinetic energy.

The axial magnetic field in the disk plane is then given by

$$B_z(r,\,0,\,0)=\frac{1}{2\pi r}\left[\frac{\partial\psi}{\partial r}\right]_{z=0,t=0}=B_0\frac{(1-r^2/a^2)}{(1+2r^2/a^2)^{5/2}}. \tag{8}$$

This field $B_z(r, 0, 0)$ has a peak value B_0 at $r=0$, reverses sign at $r=a$, and falls off as r^{-3} for large r. Because $G\to 0$ when ξ is large and negative, it is seen that the disk flux and disk B_z will also be given by Equations (7) and (8) for large t. Thus, Equation (5) effectively corresponds to having poloidal flux frozen into the disk plane with the frozen-in flux being $\psi_{\rm disk}$.

We consider v_0 to be the jet velocity. Thus, we are assuming that the jet moves monolithically at constant velocity, and so, as stated above, we are not taking into account the internal accelerations and decelerations of the jet that were discussed in Bellan (2018a). With this assumption, the jet tip is at axial location $z_{\rm tip}\simeq v_0 t$ when t is large. We now consider positive z locations that are either far in front of the jet tip so $z\gg v_0 t$ or in the jet body behind the jet tip so $0\ll z<v_0 t$. Time is always positive. We now examine these two situations in detail:

1. Far in front of the jet tip, $z-v_0 t\gg\Delta$, so $z-v_0 t\approx z$, in which case $G\to z$, giving $\psi\to\psi_{\rm vac}$. Thus at axial locations z much farther from the disk than the jet tip, the poloidal flux ψ reverts to being vacuum-like, and there are no toroidal currents.
2. In the jet body far behind the tip so $z\ll v_0 t$, the function $z-v_0 t$ will be large and negative, in which case $G\simeq 0$ and $\psi\to\psi_{\rm disk}$. Because ψ has negligible z dependence in this behind-the-tip region, the poloidal flux contours are stretched out in the z direction. This means that B_z will be given approximately by Equation (8) for the entire range of z within the jet. The jet will thus be collimated in this region because there is very weak z dependence.

The poloidal flux defined by Equation (5) therefore has the functional form of an axially stretched dipole flux such that there is no axial dependence in the stretched region. Furthermore, the stretched region has a radial dependence nearly identical to that on the disk, while at distances far in front of the jet tip, the poloidal flux is vacuum-like and thus no different from what would have existed if there had been no stretching.

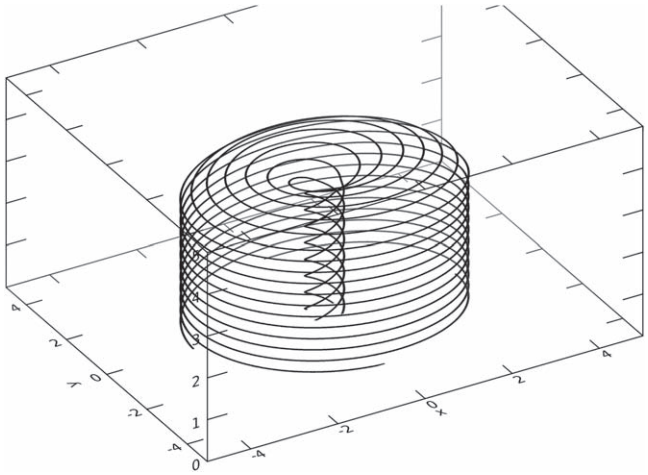

Figure 4. Plot of field lines using Equations (1) and (5) for $\bar{\lambda}=5$, $v_0 t/a=3$, and $\Delta/a=0.1$.

The poloidal flux defined by Equation (5) has been prescribed to have the additional important feature that

$$\frac{\partial\psi}{\partial t}=-v_0\frac{\partial\psi}{\partial z}, \tag{9}$$

a property that will be important for constructing solutions to Maxwell's equations.

In order to have the simplest nontrivial form for I, it is assumed that

$$\mu_0 I=\lambda\psi \tag{10}$$

where

$$\lambda=\lambda_0\tanh\left(\frac{z}{h}\right) \tag{11}$$

and h is the nominal height of the accretion disk. The simple linear dependence of I on ψ is similar to that assumed in spheromaks (Bellan 2018c) and in a model for astrophysical jets that takes into account canonical angular momentum conservation (Bellan 2017).

Figure 4 plots a typical set of field lines obtained by using Equations (5), (6), and (10) in Equation (1), while Figure 5 shows plots for a sequence of times. These plots show that at small radius, there is a collimated, twisted magnetic field having a finite axial length that increases with time. This topology and evolution are qualitatively similar to that provided by a full 3D ideal MHD model of an astrophysical jet (e.g., see Figure 3 of Kato 2007). It differs from previous analytic solutions such as in Mestel (1961), Sauty (1994), Beskin (2010), and Contopoulos (1994) as these previous solutions have no time dependence and are self-similar, so the lengthening of the jet with time is not described.

The definition of λ implies that in the disk where ψ is approximately independent of z, I depends on z via λ only. Thus in the disk, that is, where $0<z<h$, there exists a radial

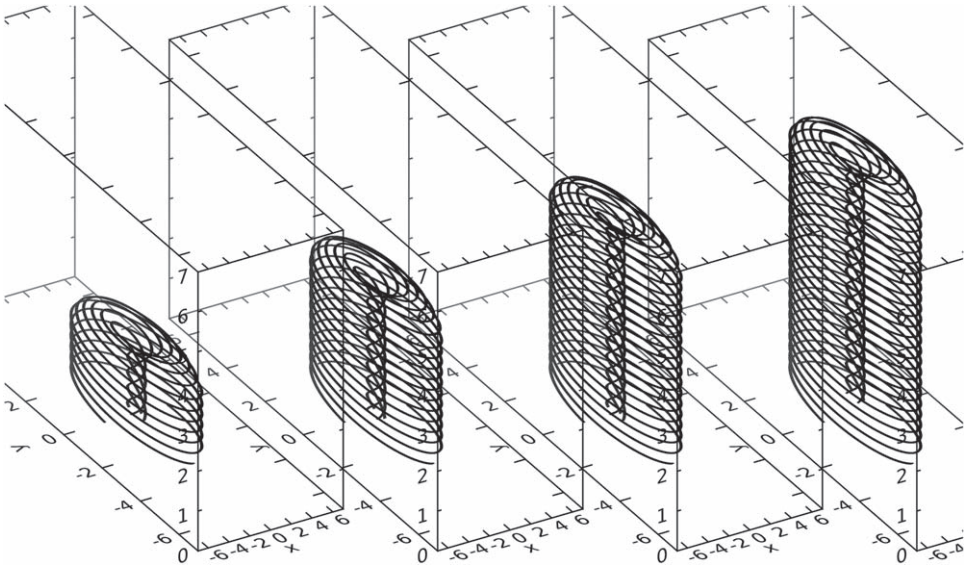

Figure 5. Plot of field lines using Equations (1) and (5) for $\bar{\lambda} = 5$ and $v_0 t/a = 1.5$, 3, 4.5, and 6.0.

current density given by

$$J_r = -\frac{1}{2\pi r}\frac{\partial I}{\partial z} = -\frac{\psi_{\rm disk}(r)}{2\pi r\mu_0}\frac{\partial \lambda}{\partial z} = -\frac{\psi_{\rm disk}(r)}{2\pi r\mu_0 h}\frac{\lambda_0}{\cosh^2(z/h)}. \tag{12}$$

At large z and in the jet, that is, $h \ll z < v_0 t$, there is an axial current density given by

$$J_z = \frac{1}{2\pi r}\frac{\partial I}{\partial r} = \frac{\lambda_0}{\mu_0}B_z. \tag{13}$$

Also at large z and in the jet, there is no radial current density because here

$$J_r = -\frac{1}{2\pi r}\frac{\partial I}{\partial z} = -\frac{\lambda_0}{2\pi\mu_0 r}\frac{\partial \psi}{\partial z} \approx 0$$

since ψ is nearly independent of z in the jet. This shows that the current is mainly in the z direction in the jet.

3. Construction of the Vector Potential

This prescription of the poloidal flux function enables determination of an axial vector potential because

$$B_\phi = -\frac{\partial A_z}{\partial r} \tag{14}$$

where a gauge has been chosen such that $A_r = 0$. Since $B_\phi = \mu_0 I/(2\pi r)$, we see that $-\partial A_z/\partial r = \lambda\psi/(2\pi r)$, so upon substitution for λ and ψ we have

$$\frac{\partial A_z}{\partial r} = -\frac{\lambda(z)B_0 a}{2}\frac{r/a}{\left(2r^2/a^2 + \left(\frac{\sqrt{2}}{a}G(z - v_0 t) + 1\right)^2\right)^{3/2}}. \tag{15}$$

This expression can be integrated to give

$$A_z(r, z, t) = \frac{\lambda(z)B_0 a^2}{4} \times \frac{1}{\left(2r^2/a^2 + \left(\frac{\sqrt{2}}{a}G(z - v_0 t) + 1\right)^2\right)^{1/2}}. \tag{16}$$

For $z \gg h$ so that Equation (11) shows that λ becomes independent of z, the time and space derivatives of Equation (16) are related by

$$\frac{\partial A_z}{\partial t} = -v_0\frac{\partial A_z}{\partial z}. \tag{17}$$

The azimuthal component of the vector potential is found by noting that the poloidal component of the magnetic field is

$$\begin{aligned}\boldsymbol{B}_{\rm pol} &= \frac{1}{2\pi}\nabla\psi \times \nabla\phi \\ &= \frac{1}{2\pi}\nabla \times (\psi\nabla\phi) \\ &= \nabla \times \left(\frac{\psi}{2\pi r}\hat{\phi}\right),\end{aligned} \tag{18}$$

so

$$A_\phi = \frac{\psi}{2\pi r}. \tag{19}$$

Thus, all three components of the vector potential have been established.

4. Construction of the Electrostatic Potential

Harris (1962) showed that the Bennett pinch could be solved in a special frame moving at the mean of the electron and ion drift velocities. The special feature of this frame, which we will call the Harris frame, is that it is possible to construct a solution of the Vlasov and Maxwell equations such that the electrostatic potential and hence the electric field are identically zero everywhere. Lorentz transformation back to the lab frame then

gives an electric field and an associated electrostatic potential in the lab frame. We assume here that the jet velocity greatly exceeds the difference J/ne between electron and ion drift velocities, so the jet velocity is nearly the same as the Harris-frame velocity. This means that in the jet frame the electric field and associated electrostatic potential are zero.

The nonrelativistic Lorentz transformation relates the jet-frame electric field $\boldsymbol{E}'$ to the lab-frame electric field $\boldsymbol{E}$ by

$$\boldsymbol{E}' = \boldsymbol{E} + \boldsymbol{v}_{\rm jet} \times \boldsymbol{B}. \tag{20}$$

Because the Harris construction in the jet frame gives $\boldsymbol{E}' = 0$, and assuming a jet velocity $\boldsymbol{v}_{\rm jet} = v_0\hat{z}$, Equation (20) gives the lab-frame radial electric field as

$$E_r = v_0 B_\phi. \tag{21}$$

Using Equation (14), the lab-frame radial electric field can then be expressed as

$$E_r = -v_0\frac{\partial A_z}{\partial r}. \tag{22}$$

Since a gauge with $A_r = 0$ has been assumed, the radial electric field $E_r = -\partial V/\partial r - \partial A_r/\partial t$ reduces to

$$E_r = -\frac{\partial V}{\partial r}. \tag{23}$$

Combining Equations (22) and (23) and integrating gives the lab-frame electrostatic potential as

$$V(r, z, t) = v_0 A_z(r, z, t), \tag{24}$$

so using Equation (16) we have

$$V(r, z, t) = \frac{v_0\lambda(z)B_0a^2}{4} \times \frac{1}{\left(2r^2/a^2 + \left(\frac{\sqrt{2}}{a}G(z - v_0t) + 1\right)^2\right)^{1/2}}. \tag{25}$$

5. Construction of the Electric and Magnetic Field Vectors

We now have sufficient information to construct the complete lab-frame electric field. Because of axisymmetry, the electrostatic potential V is independent of ϕ, so the toroidal electric field is

$$E_\phi = -\frac{\partial A_\phi}{\partial t} = -\frac{1}{2\pi r}\frac{\partial \psi}{\partial t} = \frac{v_0}{2\pi r}\frac{\partial \psi}{\partial z}; \tag{26}$$

this electric field component is missing in the static models used by Mestel (1961), Blandford & Payne (1982), Lynden-Bell (2003), and Pudritz et al. (2012); it also differs from the singular E_ϕ proposed in Contopoulos (1994).

The axial electric field in the jet region is

$$\begin{aligned} E_z &= -\frac{\partial V}{\partial z} - \frac{\partial A_z}{\partial t} \\ &= -v_0\frac{\partial A_z}{\partial z} - \frac{\partial A_z}{\partial t} \\ &= 0 \end{aligned} \tag{27}$$

where Equation (24) has been used and the last line comes from Equation (17). The radial electric field using $A_r = 0$ is given by Equation (21) as

$$E_r = v_0\frac{\lambda\psi}{2\pi r}. \tag{28}$$

The lab-frame magnetic field is

$$\begin{aligned} B_r &= -\frac{1}{2\pi r}\frac{\partial \psi}{\partial z} \\ B_\phi &= \frac{\lambda\psi}{2\pi r} \\ B_z &= \frac{1}{2\pi r}\frac{\partial \psi}{\partial r}. \end{aligned} \tag{29}$$

There is no lab-frame electric field parallel to the magnetic field since

$$\begin{aligned} \boldsymbol{E}\cdot\boldsymbol{B} &= E_rB_r + E_\phi B_\phi + E_zB_z \\ &= -v_0\frac{\lambda\psi}{2\pi r}\frac{1}{2\pi r}\frac{\partial \psi}{\partial z} - \frac{1}{2\pi r}\frac{\partial \psi}{\partial t}\frac{\lambda\psi}{2\pi r} \\ &= 0 \end{aligned} \tag{30}$$

where Equation (9) has been used.

6. Demonstration That the Time-dependent Induction Equation Is Satisfied

Because ψ is time dependent, both the electric and magnetic lab-frame fields are time dependent. This contrasts with the previous analytic models (e.g., Mestel 1961; Sauty 1994; Beskin 2010; Contopoulos 1994) where the jet fields were assumed to be independent of time and the lengthening of the jet was not taken into account. These previous analytic models assumed that the magnetic field is independent of time, so the induction equation

$$\frac{\partial \boldsymbol{B}}{\partial t} = \nabla \times (\boldsymbol{U} \times \boldsymbol{B}) \tag{31}$$

is reduced to $\nabla \times (\boldsymbol{U} \times \boldsymbol{B}) = 0$, which forces $\boldsymbol{U} \times \boldsymbol{B}$ to be the gradient of a potential. In contrast, time dependence of the magnetic field is retained here, so $\boldsymbol{U} \times \boldsymbol{B}$ is not the gradient of a potential.

Using $\boldsymbol{U} = v_0\hat{z}$, we see that

$$\begin{aligned} \boldsymbol{U} \times \boldsymbol{B} &= v_0\hat{z} \times (B_r\hat{r} + B_\phi\hat{\phi} + B_z\hat{z}) \\ &= v_0(B_r\hat{\phi} - B_\phi\hat{r}) \\ &= -\frac{v_0}{2\pi}\left(\frac{\partial \psi}{\partial z}\nabla\phi + \lambda\psi\nabla r\right), \end{aligned} \tag{32}$$

so

$$\nabla \times (\boldsymbol{U} \times \boldsymbol{B}) = \frac{v_0}{2\pi r}\left(-\frac{\partial^2\psi}{\partial r\partial z}\hat{z} + \frac{\partial^2\psi}{\partial z^2}\hat{r} - \frac{\partial}{\partial z}(\lambda\psi)\hat{\phi}\right). \tag{33}$$

Direct calculation of the time derivative of Equation (29) gives

$$\frac{\partial \boldsymbol{B}}{\partial t} = \frac{\partial}{\partial t}\left(-\frac{1}{2\pi r}\frac{\partial \psi}{\partial z}\hat{r} + \frac{\lambda\psi}{2\pi r}\hat{\phi} + \frac{1}{2\pi r}\frac{\partial \psi}{\partial r}\hat{z}\right), \tag{34}$$

which on invoking Equation (9) becomes

$$\frac{\partial \boldsymbol{B}}{\partial t} = \frac{v_0}{2\pi r}\left(\frac{\partial^2\psi}{\partial z^2}\hat{r} - \frac{\partial(\lambda\psi)}{\partial z}\hat{\phi} - \frac{\partial^2\psi}{\partial r\partial z}\hat{z}\right). \tag{35}$$

Comparison of Equations (33) and (35) shows that the time-dependent induction equation, Equation (31), is exactly satisfied.

Various points of view have been expressed on how the detailed flow moves with respect to the magnetic field. According to one point of view (e.g., Blandford & Payne 1982), the predominant flow is along magnetic field lines (beads on a wire), whereas according to another point of view, the predominant flow is an $\boldsymbol{E}\times\boldsymbol{B}$ drift. We show next that neither of these points of view is correct.

7. Particle Parallel and Drift Motion

The lab-frame particle motion can be decomposed into drifts and parallel motions superimposed on Larmor orbital motion with the main drift presumed to be the $\boldsymbol{E}\times\boldsymbol{B}$ drift. On the other hand, the particles are nearly stationary in the jet frame, with the deviation from a perfect standstill being the small relative motions between electrons and ions that constitute the electric current density. Thus, on ignoring these small deviations, the jet-frame particle velocity is assumed to be zero while the lab-frame particle velocity is

$$\boldsymbol{v}_{\rm lab}=\boldsymbol{v}_E+v_\parallel\hat{\boldsymbol{B}} \tag{36}$$

where $\boldsymbol{v}_E=\boldsymbol{E}\times\boldsymbol{B}/\mathrm{B}^2$ and $v_\parallel$ is the velocity component parallel to, that is, along the lab-frame magnetic field.

From Equation (20) we see that

$$\boldsymbol{E}=-\boldsymbol{v}_{\rm jet}\times\boldsymbol{B}=-v_0\hat{z}\times\boldsymbol{B}, \tag{37}$$

so from Equation (36) the lab-frame particle velocity is

$$\begin{aligned}\boldsymbol{v}_{\rm lab}&=\frac{(-v_0\hat{z}\times\boldsymbol{B})\times\boldsymbol{B}}{B^2}+v_\parallel\hat{\boldsymbol{B}}\\&=\frac{v_0}{B^2}(\hat{z}B^2-\boldsymbol{B}B_z)+v_\parallel\frac{\boldsymbol{B}}{B}\\&=v_0\hat{z}+\left(v_\parallel-v_0\frac{B_z}{B}\right)\frac{\boldsymbol{B}}{B}.\end{aligned} \tag{38}$$

Equation (38) shows that in order to have $\boldsymbol{v}_{\rm lab}=v_0\hat{z}$, the velocity parallel to the magnetic field must be

$$v_\parallel=v_0\frac{B_z}{B}. \tag{39}$$

Because

$$\boldsymbol{E}=v_0\frac{\lambda\psi}{2\pi r}\hat{\boldsymbol{r}}-\frac{1}{2\pi r}\frac{\partial\psi}{\partial t}\hat{\boldsymbol{\phi}}=v_0\frac{\lambda\psi}{2\pi r}\hat{\boldsymbol{r}}+\frac{v_0}{2\pi r}\frac{\partial\psi}{\partial z}\hat{\boldsymbol{\phi}}, \tag{40}$$

the $\boldsymbol{E}\times\boldsymbol{B}$ drift is

$$\begin{aligned}\boldsymbol{v}_E&=\frac{\left(\frac{v_0\lambda}{2\pi r}\psi\hat{\boldsymbol{r}}+\frac{v_0}{2\pi r}\frac{\partial\psi}{\partial z}\hat{\boldsymbol{\phi}}\right)\times\left(-\frac{1}{2\pi r}\frac{\partial\psi}{\partial z}\hat{\boldsymbol{r}}+\frac{\lambda\psi}{2\pi r}\hat{\boldsymbol{\phi}}+\frac{1}{2\pi r}\frac{\partial\psi}{\partial r}\hat{\boldsymbol{z}}\right)}{\left(\frac{1}{2\pi r}\frac{\partial\psi}{\partial z}\right)^2+\left(\frac{\lambda\psi}{2\pi r}\right)^2+\left(\frac{1}{2\pi r}\frac{\partial\psi}{\partial r}\right)^2}\\&=v_0\frac{\frac{\partial\psi}{\partial z}\frac{\partial\psi}{\partial r}\hat{\boldsymbol{r}}-\lambda\psi\frac{\partial\psi}{\partial r}\hat{\boldsymbol{\phi}}+\left(\left(\frac{\partial\psi}{\partial z}\right)^2+\lambda^2\right)\hat{\boldsymbol{z}}}{\left(\frac{\partial\psi}{\partial z}\right)^2+\lambda^2\psi^2+\left(\frac{\partial\psi}{\partial r}\right)^2}.\end{aligned} \tag{41}$$

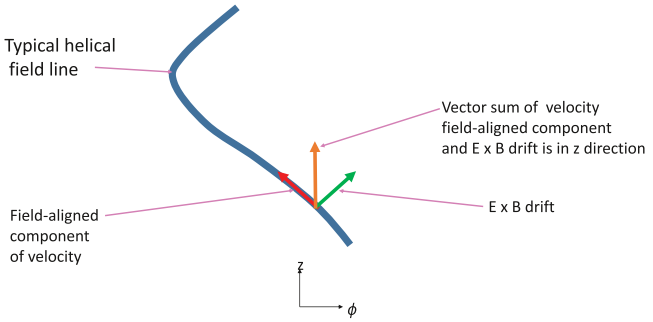

Figure 6. Zoomed-in view of helical field (blue). The field-aligned component of the velocity (beads-on-a-string part) and the $\boldsymbol{E}\times\boldsymbol{B}$ drift add vectorially to give a velocity purely in the z direction. The ϕ components cancel, so there is no centrifugal force.

The velocity parallel to the magnetic field is

$$\begin{aligned}v_\parallel\hat{\boldsymbol{B}}&=v_0\frac{\frac{1}{2\pi r}\frac{\partial\psi}{\partial r}}{\left(-\frac{1}{2\pi r}\frac{\partial\psi}{\partial z}\right)^2+\left(\frac{\lambda\psi}{2\pi r}\right)^2+\left(\frac{1}{2\pi r}\frac{\partial\psi}{\partial r}\right)^2}\\&\quad\times\left(-\frac{1}{2\pi r}\frac{\partial\psi}{\partial z}\hat{\boldsymbol{r}}+\frac{\lambda\psi}{2\pi r}\hat{\boldsymbol{\phi}}+\frac{1}{2\pi r}\frac{\partial\psi}{\partial r}\hat{\boldsymbol{z}}\right)\end{aligned} \tag{42}$$

$$=v_0\frac{\frac{\partial\psi}{\partial r}}{\left(\frac{\partial\psi}{\partial z}\right)^2+\lambda^2\psi^2+\left(\frac{\partial\psi}{\partial r}\right)^2}\left(-\frac{\partial\psi}{\partial z}\hat{\boldsymbol{r}}+\lambda\psi\hat{\boldsymbol{\phi}}+\frac{\partial\psi}{\partial r}\hat{\boldsymbol{z}}\right). \tag{43}$$

Equations (41) and (42) show that when $\boldsymbol{v}_E$ and $v_\parallel\hat{\boldsymbol{B}}$ are added, the r and ϕ components cancel and the z components sum to give just $v_0\hat{z}$.

Thus, the motion is neither along the magnetic field (as in "beads on a wire") nor an $\boldsymbol{E}\times\boldsymbol{B}$ drift but rather is a sum of both these types of motion. This is shown schematically in Figure 6. Notably, there is no azimuthal particle velocity even though both the $\boldsymbol{E}\times\boldsymbol{B}$ drift and the parallel to the magnetic field motion have azimuthal components. In the main jet body where B_z is positive, $v_\parallel$ is positive and thus is in the positive z direction. It is also noteworthy that in the exterior region where B_z is negative, $v_\parallel$ is also negative, so $v_\parallel\hat{\boldsymbol{B}}$ remains in the positive z direction. Thus, it is not correct to picture a particle as following a magnetic field line, nor is it correct to picture a particle as having only an $\boldsymbol{E}\times\boldsymbol{B}$ drift. The particle has both motions, and what results differs from both. Also, it is seen that the axial motion of the particle can be decomposed into a contribution from motion along the magnetic field (z component of Equation (42)) and a contribution from the $\boldsymbol{E}\times\boldsymbol{B}$ drift (z component of Equation (41)). This demonstration that the flow is not along the magnetic field shows that images of the flow cannot be used as representations of the magnetic field direction. Because the ϕ component of $v_\parallel\hat{\boldsymbol{B}}$ and the ϕ component of the $\boldsymbol{E}\times\boldsymbol{B}$ drift cancel, there is no azimuthal velocity and so no centrifugal force. Because this test particle motion is the same for both electrons and ions, it is equivalent to the center-of-mass velocity of the MHD plasma.

This particle drift analysis shows that the electric and magnetic fields constructed here are consistent with Maxwell's equations and also with the particle drift equations, which are essentially an approximate solution to the Lorentz force equation. Furthermore, the analysis shows that the electric field has the precise form to provide a lab-frame $\boldsymbol{E}\times\boldsymbol{B}$ drift

across the magnetic field consistent with the jet motion. Even though this $\boldsymbol{E}\times\boldsymbol{B}$ drift has r and ϕ components, the motion along the magnetic field is just such as to cancel these r and ϕ components. The strict axial motion was prescribed and does not exclude the possibility that a situation could have had a rotating component; this analysis shows that a rotating component is not required. However, as discussed in Bellan (2017), the gas in the disk feeding the jet is presumed not to have a significant azimuthal velocity because of magnetic braking removing the angular momentum of the accreting material via the torque in the disk plane associated with $(\boldsymbol{J}\times\boldsymbol{B})_\phi = -J_r B_z$. It should also be noted that near the disk the magnetic force component $(\boldsymbol{J}\times\boldsymbol{B})_z = J_r B_\phi = -\partial/\partial z(B_\phi^2/2\mu_0)$ is directed so as to confine pressure on the disk because Equations (1), (10), and (11) show that B_ϕ is an odd function of z, and so B_ϕ^2 increases on moving away from the disk plane. Equation (30) shows that the constructed field is in agreement with the ideal MHD prescription that there be no electric field parallel to the magnetic field.

An important conclusion of this analysis is that because there is an electrostatic potential gradient in the radial direction, there must necessarily be an electrostatic potential difference between the ends of a magnetic field line. Here "ends" means the two locations where a given field line intercepts the $z = 0$ plane; one end is at $r < a$ and the other is at $r > a$. In the jet body (i.e., at a position $0 \ll z \ll v_0 t$), Equation (25) prescribes that the electrostatic potential has the form

$$V(r, z, t) = \frac{v_0\lambda_0 B_0 a^2}{4}\,\frac{1}{(2r^2/a^2+1)^{1/2}}. \tag{44}$$

This means that in the jet main body the inner magnetic field lines (i.e., field lines with $r < a$) are each at an equipotential, but the outer region (i.e., $r > a$) of these same magnetic field lines is at a different equipotential because of the r dependence of V.

This radial electrostatic potential drop can be considered as being the voltage drop from a battery where one terminal of the battery is connected to the inner segment of a magnetic field line at $r < a$ near $z = 0$ and the other terminal of the battery is connected to the outer segment of the same field line at $r > a$ and also near $z = 0$. This voltage corresponds to the rate of injection of toroidal flux into the system. This electrostatic potential is implicit in the MHD equations but not explicitly mentioned because these equations involve only the curl of the electric field. Helicity considerations show that such an electrostatic potential is required to inject helicity into a volume (see Jarboe et al. 1983; Jensen & Chu 1984; Bellan 2018c). Because the jet length is continuously increasing and because the jet magnetic field is helical, there is an injection of helicity. Equation (44) implies that the electric field is pointing radially outward, which implies that the disk is acting as a power source for the jet since J_r is pointing radially inward and $\boldsymbol{J}\cdot\boldsymbol{E} < \boldsymbol{0}$ corresponds to sourcing electric power. A gravity-driven mechanism for providing this electrical power source was proposed in Bellan (2008, 2016, 2017).

8. Radial Force Balance and Pressure Profile in the Jet Main Body

The jet main body is defined as the region $0 \ll z \ll v_0 t$. In this region, G as defined in Equation (6) is nearly zero, so the poloidal flux is essentially the disk flux as prescribed by Equation (7). Because there is effectively no z dependence in the main body, Equation (29) gives the main-body magnetic field as

$$\begin{aligned} B_r &= 0\\ B_\phi &= \frac{\lambda\psi}{2\pi r}\\ B_z &= \frac{1}{2\pi r}\frac{\partial\psi}{\partial r}. \end{aligned} \tag{45}$$

The current density is then given by

$$\begin{aligned} \mu_0 J_r &= 0\\ \mu_0 J_\phi &= -\frac{\partial B_z}{\partial r}\\ \mu_0 J_z &= \frac{1}{r}\frac{\partial}{\partial r}(rB_\phi). \end{aligned} \tag{46}$$

Since the velocity is constant and in the z direction, the main-body MHD equation of motion reduces to

$$\nabla P = \boldsymbol{J}\times\boldsymbol{B}. \tag{47}$$

Because $I = I(\psi)$, the ϕ components of both sides of Equation (47) vanish. Furthermore, there is no z component of $\boldsymbol{J}\times\boldsymbol{B}$ since J_r and B_r both vanish. Thus, only the radial component has nonvanishing left and right sides. The radial component is

$$\begin{aligned} \frac{\partial P}{\partial r} &= J_\phi B_z - J_z B_\phi\\ &= -\frac{1}{8\pi^2\mu_0}\left(\frac{\lambda^2}{r^2}\frac{\partial\psi^2}{\partial r} + \frac{\partial}{\partial r}\left(\frac{1}{r}\frac{\partial\psi}{\partial r}\right)^2\right). \end{aligned} \tag{48}$$

The radial pressure profile is obtained by integrating Equation (48). To do this, it is convenient to define $s = r/a$ and $\bar{\lambda} = \lambda a$ so Equation (7) can be expressed as

$$\psi(s) = B_0\pi a^2\bar{\psi}(s) \tag{49}$$

where

$$\bar{\psi}(s) = \frac{s^2}{(2s^2+1)^{3/2}}. \tag{50}$$

Equation (48) then becomes

$$\begin{aligned} \frac{\partial P}{\partial s} &= -\frac{B_0^2}{2\mu_0}\left(\frac{\bar{\lambda}^2}{4s^2}\frac{\partial\bar{\psi}^2}{\partial s} + \frac{1}{4}\frac{\partial}{\partial s}\left(\frac{1}{s}\frac{\partial\bar{\psi}}{\partial s}\right)^2\right)\\ &= -\frac{B_0^2}{2\mu_0}\frac{\partial}{\partial s}\left(\frac{\bar{\lambda}^2}{16}\frac{(2s^2-1)}{(2s^2+1)^3} + \frac{(s^2-1)^2}{(2s^2+1)^5}\right), \end{aligned} \tag{51}$$

which can also be expressed as

$$\frac{\partial P}{\partial s} = \frac{B_0^2}{2\mu_0}\frac{s(s^2-1)}{(2s^2+1)^6}(\bar{\lambda}^2(2s^2+1)^2 + 12(s^2-2)), \tag{52}$$

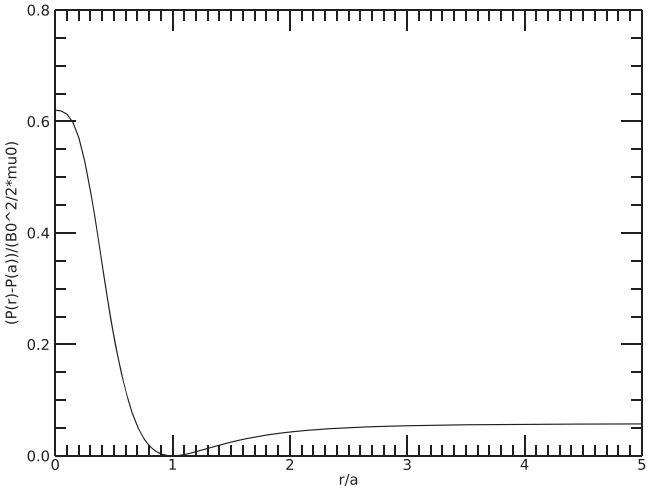

Figure 7. Plot of $[P(s) - P(1)]/(B_0^2/2\mu_0)$ for $\bar{\lambda} = 5$.

which shows that $\partial P/\partial s$ vanishes at $s = 0$, $s = 1$, and $s = \infty$. Integration of Equation (51) gives

$$P(s) = P(1) - \frac{B_0^2}{2\mu_0}\left(\frac{\bar{\lambda}^2}{16}\left(\frac{(2s^2-1)}{(2s^2+1)^3} - \frac{1}{27}\right) + \frac{(s^2-1)^2}{(2s^2+1)^5}\right). \quad (53)$$

Equation (53) shows that the pressure peaks on axis, has a minimum at $r/a = 1$, and then rises to a small constant as $r/a \to \infty$. The pressure given by Equation (53) is plotted in Figure 7 for $\bar{\lambda} = 5$. At $r = \infty$, the pressure is

$$P(\infty) = P(1) + \frac{B_0^2}{2\mu_0}\frac{\bar{\lambda}^2}{432} \quad (54)$$

while at $s = 0$ the pressure is

$$P(0) = P(1) + \frac{B_0^2}{2\mu_0}\left[\frac{7}{108}\bar{\lambda}^2 - 1\right]. \quad (55)$$

Equation (55) indicates that it is necessary to have $|\bar{\lambda}| > \sqrt{108/7} = 3.93$ in order to have the pressure peak on the z-axis. The magnetic field is force-free at the locations where the pressure gradient vanishes and, in particular, is force-free at $r = a$. This pressure profile is more realistic than a simple parabolic profile where $P \sim 1 - r^2/a^2$ for $r < a$ and $P = 0$ for $r > a$ because such a profile would have a physically unrealistic, discontinuous derivative at $r = a$. The radial component of the $\boldsymbol{J} \times \boldsymbol{B}$ force is thus radially inward for $r < a$ and radially outward for $r > a$. Near the axis, the poloidal current provides an inward pinch force, but for $r > a$ there is a repulsive force between the forward current flowing in the positive z direction at small r and the return current flowing in the negative z direction at large r. This can be understood in an equivalent manner by noting that B_ϕ has the same sign at all r since $B_\phi = \mu_0 I/2\pi r$ and I is the total enclosed current in a circle of radius r, whereas $J_z \sim \lambda B_z \sim r^{-1}\,\partial\psi/\partial r$ reverses direction at $r = a$, which is the radius at which ψ is at a maximum.

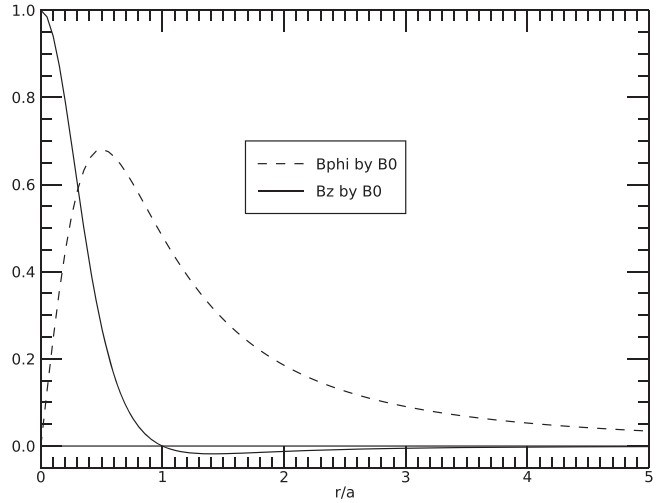

Figure 8. Plots of B_ϕ/B_0 and $B_{z/}\,B_0$ for $\bar{\lambda} = 5$.

The magnetic field components B_ϕ and B_z can be expressed in dimensionless form as

$$\frac{B_\phi}{B_0} = \frac{\bar{\lambda}}{2}\frac{r/a}{(2r^2/a^2+1)^{3/2}}$$
$$\frac{B_z}{B_0} = \frac{1 - r^2/a^2}{(2r^2/a^2+1)^{\frac{5}{2}}}. \quad (56)$$

These field components are plotted in Figure 8 and can be compared to the pressure profile in Figure 7. It is seen that at large r, B_ϕ decays as $1/r^2$, whereas B_z decays as $1/r^3$, so B_ϕ becomes relatively larger, which is also evident in Figure 4, where it is seen that the field lines are more twisted in the $r \gg a$ outer region than in the inner jet region where $r < a$. However, the pressure is nearly flat in this outer region, indicating that there is negligible magnetic force in this outer region, as is consistent with the magnetic fields being extremely small in the outer region.

9. Comparison to Previous Models

There have been a large number of previous analytical models of jets; a comparison will now be provided to several representative examples of these previous models.

1. Li (1996) presented an analytic model of relativistic jet formation assuming stationary magnetic fields, ignored the poloidal field, and did not take into account that the jet has a finite length that is increasing with time.
2. Tsinganos (2007) presented an analytic model for nonrelativistic winds and jets. This model contained both toroidal and poloidal fields but again assumed a stationary solution and did not take into account that the jet has a finite length that is increasing with time. Self-similar solutions having a magnetic flux extending to infinity were proposed. This is in contrast to the model presented here where the magnetic field is not assumed to be stationary, a time-dependent poloidal field is taken into account, the jet has a finite length that is increasing with time, and the fields are not self-similar.
3. Vlahakis & Tsinganos (1999) examined what were claimed to be exact and self-consistent MHD solutions that described steady and axisymmetric hydromagnetic

outflows; by steady it was assumed that $\partial/\partial t = 0$, that is, the fields were assumed to be stationary, so no account was taken of the jet length increasing with time.

4. Section 2 of Sauty (1994) discusses the framework of astrophysical wind and jet theories and the approximations often employed in the literature but remarks that these approximations are not always justified. In particular, Section 2.1.4 addresses the validity of the approximations of axisymmetry and stationarity and states "La stationnarité n'est pas toujours respectée puisque des mouvements propres sont mesurés dans les nodules des jets d'étoiles jeunes" (translation: "Stationarity is not always respected since proper motions are measured in the nodules of the jets from young stars"). The section goes on to state that nevertheless there exists a large-scale global structure that is permanent and axisymmetric. The claim that the global structure is permanent does not take into account that the length of jets increases with time, that is, that the structure is neither permanent nor stationary. The last sentence (translated) in this section states that "the nonstationary numerical simulations of jets have highlighted the necessity of developing stationary models as a basis for the study of nonstationary effects." Such a presumption is clearly incorrect when nonstationary physics qualitatively differs from stationary physics, as is the case for Faraday's law. Developing a stationary model for the electric field (i.e., a model of electrostatic electric fields) does not provide a basis for the study of inductive electric fields (i.e., electric fields produced by a time-dependent magnetic field). Stationary electric fields require finite charge density (i.e., matter), have zero curl, and can be expressed as the gradient of a potential, whereas inductive electric fields can exist in vacuum, have finite curl, and cannot be expressed as the gradient of a potential. Thus, contrary to Sauty (1994), the study of stationary electric fields does not provide a basis for the study of inductive electric fields, so the study of stationary models does not provide a basis for the study of nonstationary models.
5. Salmeron et al. (2011) discussed outflows from accretion disks assuming steady-state MHD equations and thus did not take into account that the jet length is increasing with time.
6. Sauty et al. (2011) modeled T Tauri jets and assumed stationary MHD equations and thus did not take into account that the jet length is increasing with time.
7. Breitmoser & Camenzind (2000) presented a relativistic model of outflows and assumed that the solution was time independent, so the lengthening of the jet with time was not taken into account.
8. Blandford & Payne (1982) discussed outflows assuming a stationary solution and constructed a self-similar description. Blandford & Payne (1982) invoked a "beads-on-a-wire" analog wherein fluid elements initially undergoing Keplerian rotation when on the disk (i.e., at $z = 0$) slide off the disk while being constrained to stay on a field line that has radius r increasing with axial displacement from the disk; the fluid element thus is like a bead on a helical wire with displacement r from the symmetry axis increasing with distance z. The beads-on-a-wire argument in Blandford & Payne (1982) is based on Ferraro's law of isorotation. This law assumes a stationary solution and states that the fluid elements, like beads on a rigid rotating wire, move with constant angular velocity as they move along a surface of constant poloidal flux. However, Ferraro's law of isorotation is based on assumptions that do not hold in the situation under consideration even if a stationary solution were to be assumed, because the magnetic field is helical and there are both axial and azimuthal velocity components. Ferraro's law of isorotation requires that the velocity be strictly toroidal, that the magnetic field be strictly poloidal, and that the system is time independent. Thus, Ferraro's law of isorotation assumes $\boldsymbol{U} = r\omega(r, z)\hat{\phi}$ and $\boldsymbol{B} = (2\pi r)^{-1}\nabla\psi \times \hat{\phi}$, so the time-independent induction equation reduces to

$$\nabla \times (\boldsymbol{U} \times \boldsymbol{B}) = \nabla \times (r\omega(r, z)\hat{\phi} \times [(2\pi r)^{-1}\nabla\psi \times \phi]) \quad (57)$$

$$= \frac{1}{2\pi}\nabla \times \omega\nabla\psi \quad (58)$$

$$= \frac{1}{2\pi}\nabla\omega \times \nabla\psi \quad (59)$$

$$= 0; \quad (60)$$

this implies $\omega = \omega(\psi)$ so all points on a poloidal flux surface rotate at the same velocity (i.e., isorotate). However, this is not true in the more general case where both the velocity and the magnetic field have both poloidal and toroidal components. As in Mestel (1961) in the more general case where $\boldsymbol{U} = \omega r\hat{\phi} + \boldsymbol{U}_p$ and $\boldsymbol{B} = B_\phi\phi + (2\pi r)^{-1}\nabla\psi \times \hat{\phi}$, the time-independent induction equation involves both the curl of a poloidal term

$$\nabla \times (\boldsymbol{U}_p \times \boldsymbol{B}_t + \boldsymbol{U}_t \times \boldsymbol{B}_p) = 0 \quad (61)$$

and the curl of a toroidal term

$$\nabla \times (\boldsymbol{U}_p \times \boldsymbol{B}_p) = 0. \quad (62)$$

Solution of Equation (62) gives $\boldsymbol{U}_p = \kappa\boldsymbol{B}_p$ because axisymmetry precludes $\boldsymbol{U}_p \times \boldsymbol{B}_p$, which is in the toroidal direction, from being a finite gradient of a potential. Substitution of $\boldsymbol{U}_p$ into Equation (61) gives

$$\nabla \times \left(\frac{\kappa}{2\pi r}(\nabla\psi \times \hat{\phi}) \times B_\phi\hat{\phi} + \omega r\hat{\phi} \times [(2\pi r)^{-1}\nabla\psi \times \hat{\phi}]\right) = 0, \quad (63)$$

so

$$\nabla \times \left(\left(-\frac{\kappa B_\phi}{r} + \omega\right)\nabla\psi\right) = 0. \quad (64)$$

This implies

$$\omega - \frac{\kappa B_\phi}{r} = \alpha(\psi), \quad (65)$$

so if there is finite poloidal motion and a helical magnetic field (i.e., both κ and B_ϕ are finite), then ω is not constant on a flux surface, and thus Ferraro's law of isorotation does not hold. Thus, beads do not move with constant angular velocity along a helical wire because the spatial dependence of B_ϕ has not been constrained and κ is nonzero if the beads are moving along the field.

9. Lynden-Bell (2003) did not include dynamics and assumed that a jet is a force-free magnetic bubble that pushes against external hydrodynamic pressure. Because of the force-free property, the magnetic field is helical with topology similar to that presented here. However, because of the force-free assumption, there is no peaking of pressure on the jet axis, in contrast to the result given in Section 8 here.
10. Mestel (1961) assumed time independence and worked out relations between velocity and magnetic field with no specified boundary conditions at $z = 0$.

A common feature of the previous models listed above is the assumption that the system is stationary, so the MHD induction equation $\partial \boldsymbol{B}/\partial t = \nabla \times (\boldsymbol{U} \times \boldsymbol{B})$ reduces to $\nabla \times (\boldsymbol{U} \times \boldsymbol{B}) = 0$, whereas in the model presented here the time derivative is retained and a nontrivial solution to the time-dependent induction equation is obtained. Another common feature of the papers in the above list is that the length of the jets is never specified, which is not logical because jets have a velocity and a starting time, so the length should be given by the velocity times the time interval elapsed since the starting time; that is, the jet length is $l \sim vt$. Because the base of the jet is anchored in an accretion disk, the base is stationary, so the ratio of the jet length to the radius of the jet base increases with time. This means that the jet aspect ratio changes with time, so the jet is neither stationary nor self-similar. Since magnetic flux is frozen into the jet, the magnetic flux must also be time dependent and not self-similar. The only place where the magnetic field is stationary is the disk plane. The model presented here has a poloidal flux that is time independent in the disk plane but time dependent above the disk plane; this is consistent with the poloidal field being anchored in the disk and stretching out as the jet lengthens.

When one considers the time-dependent interaction between the MHD equation of motion and the MHD induction equation for given initial conditions on $\boldsymbol{U}$ and on $\boldsymbol{B}$, it is seen that the equation of motion advances $\boldsymbol{U}$ in time and the induction equation advances $\boldsymbol{B}$ in time. Thus, given an initial $\boldsymbol{U}$ and $\boldsymbol{B}$, the equation of motion updates $\boldsymbol{U}$ after a time step dt. The ideal MHD Ohm's law instantaneously creates an electric field $\boldsymbol{E} = -\boldsymbol{U} \times \boldsymbol{B}$, which upon insertion into Faraday's law provides the induction equation that updates $\boldsymbol{B}$ after a time step dt. The time-dependent induction equation imposes no constraint on $\boldsymbol{U}$ as $\boldsymbol{U}$ is just an input to this equation. The behavior of $\boldsymbol{U}$ is entirely determined by the equation of motion, which is the equation that contains the time derivative of $\boldsymbol{U}$. Numerical codes are constructed according to this logic and do not have any built-in constraints, such as Ferraro's law of isorotation, on the form of $\boldsymbol{U}$.

A variant on the models listed above is the work by Contopoulos (1994), who constructed an axisymmetric poloidal flux function that was stationary but nevertheless implied a toroidal electric field $E_\phi = \alpha/r$ where α is a constant. However, this is nonphysical because it implies a singular electric field on the z-axis, but the z-axis is an important part of an actual jet. This violates the regularity condition for real physical quantities as discussed by Lewis & Bellan (1990). Contopoulos (1994) admits that this $E_\phi \sim 1/r$ solution is nonphysical but proposes that it might be valid in a domain excluding the axis for a limited time duration. However, introducing the concept of a limited time duration is inconsistent with the assumption that the system is stationary. The proposed accumulation of poloidal flux that generates a constant rE_ϕ for finite r is in fact the essence of the tokamak fusion device, which works because the tokamak is doubly connected, that is, has a doughnut shape with a hole in the middle having an increasing flux provided by coils in this hole. However, it is well known that the flux in the hole cannot increase indefinitely, so the system is not stationary. The tokamak topology is not the correct analog for an astrophysical jet because the domain of an astrophysical jet is not doubly connected, that is, one cannot exclude the axis.

The model presented here does not attempt to describe the axial forces that lead to the jet axial motion nor does it attempt to describe the power source driving the jet. Descriptions for how magnetic and hydrodynamic forces cause jet axial motion are given in Bellan (2018a, 2018b). How angular momentum is absorbed by magnetic braking in the disk, then convected by the jet, and finally shed elsewhere is discussed in Bellan (2016, 2017); these papers also discuss how accretion converts gravitational potential energy into the electrical power supply that drives the electric current in the jet.

Certain previous analytic models, such as the models by Blandford & Payne (1982) and Contopoulos (1994), have magnetic field lines that are presumed to extend to infinity according to various power laws that are calculated from a set of differential equations. However, unless the nonphysical assumption of electric currents at infinity is invoked, the region at infinity must be far from all regions containing an electric current. Since electric currents produce only dipole or higher order multipole magnetic fields and since multipoles of order higher than a dipole decay with distance at a greater rate than a dipole field, the field at large distances must be that of a dipole, that is, the field that is prescribed by Equation (5) in the limit that z approaches infinity. At large radii, the dipole field lines are prescribed in spherical polar coordinates $\{R, \theta, \phi\}$ by $R = R_0 \sin^2\theta$, where θ is the polar angle and R_0 is the radius at which the field line intercepts the disk plane. The disk plane has $\theta = \pi/2$, which corresponds to the $z = 0$ plane when cylindrical coordinates $\{r, \phi, z\}$ are used (see p. 166 of Kivelson & Russell 1995) and $R = \sqrt{r^2 + z^2}$ while $\sin\theta = r/R$. This dipole field $R = R_0 \sin^2\theta$ is the limiting form of Equation (5) when $z \gg a, vt$; any other prescription would imply the existence of nonphysical currents at infinity.

Numerical simulations of astrophysical jets have been made by a number of authors, notable examples being Stone & Norman (1992), Ouyed & Pudritz (1997), Kato (2007), Nakamura et al. (2010), and Zhai et al. (2014). Unlike the previous analytic models, the numerical simulations typically allow for time dependence and do not invoke self-similarity. The numerical simulations produce jets with helical field lines that become longer with time, and the model presented here is qualitatively and topologically consistent with these numerical simulations. For example, Figure 3 of the 3D numerical MHD solution in Kato (2007) is topologically identical to Figure 4 here. A feature of numerical simulations is that there is complete discretion regarding imposed boundary conditions, so the numerical domain may or may not have field lines exiting the boundaries. The 3D numerical simulation by Zhai et al. (2014) had boundary conditions consistent with Equation (5) and gave results qualitatively and topologically consistent with the model proposed here and quantitatively consistent with laboratory experiments.

Table 1
Comparison of This Model to Mestel (1961), Pudritz et al. (2012), Blandford & Payne (1982), Lynden-Bell (2003), and Bellan (2017)

	This Model	Mestel Pudritz	Blandford & Payne	Lynden-Bell	Bellan (2017)
Time-dependent flux	yes	no	no	no	yes
Disk boundary condition	yes	no	yes	yes	yes
Self-similar	no	yes	yes	no	no
Jet lengthens with time	yes	no	no	yes	yes
Inductive $\boldsymbol{E}$	yes	no	no	no	yes
Electrostatic $\boldsymbol{E}$	yes	yes	no	no	yes
Voltage drop along $\boldsymbol{B}$ line	yes	no	no	no	yes
$\boldsymbol{E}\cdot\boldsymbol{B}=0$ everywhere	yes	yes	yes	yes	yes
Acceleration in main body	no	no	yes	no	yes
Deceleration at jet tip	no	no	no	no	yes
Collimation dynamics	no	no	no	no	yes
On-axis peak pressure	yes	no	no	no	yes
Radial pressure to ∞	yes	no	no	yes	no
Beads-on-a-wire picture	no	no	yes	no	no
Compressible	yes	no	no	no	yes

The model presented here has no rotation but does not preclude rotation. Recently, Lavine & You (2019) have shown that a helical shear (i.e., rotation at different angular velocities at different radii and different axial velocities at different radii) prevents the development of kink instabilities, so very long and stable collimated jets result.

10. Discussion and Conclusions

Table 1 summarizes the similarities and differences between the model presented here and representative previous models. The model presented here takes into account the electrostatic potential that injects toroidal flux into a lengthening, current-carrying jet. This is known in spheromak research (Jarboe et al. 1983; Jensen & Chu 1984; Bellan 2018c) but has not received much attention in the astrophysical literature. It is also an aspect of Poynting flux power injection where the Poynting flux is $P = E_r B_\phi/\mu_0$ and E_r is from the radial voltage drop while B_ϕ is from the axial current. The lengthening of the jet requires power injection because a long jet has more internal magnetic energy and more total kinetic energy than a short jet. The model assumes that the jet is effectively a spear-like, rigid body that is penetrating the half volume above the accretion disk, that is, the half volume where $z > 0$. In contrast, Bellan (2017) shows that the jet velocity actually varies with axial position, accelerating on leaving the disk but then partially decelerating at the tip; this is somewhat like the tip of a flexible spear being squashed as the spear encounters headwinds and this squashing acting to collimate the spear. Bellan (2017) also showed that the jet transports angular momentum even though the jet itself does not need to be rotating; this is in analogy to wires transporting angular momentum from an electric generator to a distant electric motor that rotates a load.

Because this analytic construction assumes a uniform axial velocity, it misses the details of acceleration and deceleration within the jet (the squashing of the spear tip in the analogy given above). In compensation, the model captures the effects of the time-dependent magnetic field, the increasing length of the jet, the radial balance between magnetic and hydrodynamic pressure forces, and the distinction between the high-current, high-pressure, high-field situation within the jet and the situation exterior to the jet where all these quantities are either much smaller or vacuum-like. These captured effects show that there is a radial electrostatic potential drop in the disk, that the jet pressure peaks on axis but drops to a minimum where B_z reverses direction and then climbs to a small constant value at large radius.

Consideration of particle motion shows that plasma does not in general flow along a field line like a bead on a wire. Instead, the plasma flow is the vector sum of the field-aligned motion and the cross-field drift. Because the magnetic field is helical, there is a cancellation between the azimuthal component of the field-aligned motion (beads-on-a-wire component) and the azimuthal component of the $\boldsymbol{E}\times\boldsymbol{B}$ drift, with the result that the plasma motion is purely axial.

The time-dependent helical magnetic structure has increasing length and an associated electric field; these magnetic and electric fields satisfy Faraday's law. Thus the fields and motions satisfy the time-dependent induction equation, a feature missing from previous analytic models. The net time-dependent electric field (inductive plus electrostatic components) is perpendicular to the time-dependent magnetic field, so $\boldsymbol{E}(r, z, t)\cdot\boldsymbol{B}(r, z, t) = 0$ everywhere at all times.

There is an electrostatic potential drop along a magnetic field line but no electric field along the field line. This seemingly contradictory situation exists because the inductive and electrostatic components of the parallel electric field cancel each other. The radial electrostatic potential drop corresponds to the rate of increase of toroidal flux in the jet as a result of the jet getting longer. While this discussion has been done in the framework of astrophysical jets, it should also be relevant to solar corona structures having similar morphology. It is also relevant to spheromak formation (Jarboe et al. 1983; Bellan 2018c) and to the use of spheromak methods in magnetized target fusion (Howard et al. 2009; Seo & Bellan 2018).

This material is based upon work supported by the NSF/DOE Partnership in Plasma Science and Engineering via U.S. Department of Energy Office of Science, Office of Fusion Energy Sciences via Award Number DE-FG02-04ER54755, by the USDOE ARPA-E via Award Number DE-AR0000565, by the Air Force Office of Scientific Research via Award Number FA9550-11-1-0184, and by the National Science Foundation Division of Atmospheric and Geospace Sciences via Award Number 1914599.

ORCID iDs

P. M. Bellan https://orcid.org/0000-0002-0886-8782

References

Bellan, P. M. 2008, ApJ, 687, 311
Bellan, P. M. 2016, MNRAS, 458, 4400
Bellan, P. M. 2017, PPCF, 60, 014006
Bellan, P. M. 2018a, PhPl, 25, 055601
Bellan, P. M. 2018b, JPlPh, 84, 755840501
Bellan, P. M. 2018c, Magnetic Helicity, Spheromaks, Solar Corona Loops, and Astrophysical Jets (London: World Scientific)
Bennett, W. H. 1934, PhRv, 45, 890
Beskin, V. S. 2010, PhyU, 53, 1199
Blandford, R. D., & Payne, D. G. 1982, MNRAS, 199, 883
Breitmoser, E., & Camenzind, M. 2000, A&A, 361, 207
Ciardi, A., Lebedev, S. V., Frank, A., et al. 2007, Ap&SS, 307, 17
Contopoulos, J. 1994, ApJ, 432, 508
Curtis, H. 1918, PLicO, 13, 9
Dal Pino, E. M. D. 2005, AdSpR, 35, 908
Gourdain, P.-A., & Seyler, C. E. 2014, PPCF, 56, 035002
Harris, E. G. 1962, NCim, 23, 115
Henriksen, R. N., & Rayburn, D. R. 1971, MNRAS, 152, 323
Howard, S., Laberge, M., McIlwraith, L., Richardson, D., & Gregson, J. 2009, Journal of Fusion Energy, 28, 156
Hsu, S. C., & Bellan, P. M. 2002, MNRAS, 334, 257
Huarte-Espinosa, M., Frank, A., Blackman, E. G., et al. 2013, HEDP, 9, 264
Jarboe, T. R., Henins, I., Sherwood, A. R., Barnes, C. W., & Hoida, H. W. 1983, PhRvL, 51, 39
Jensen, T. H., & Chu, M. S. 1984, PhFl, 27, 2881
Kato, Y. 2007, Ap&SS, 307, 11
Kivelson, M. G., & Russell, C. T. 1995, Introduction to Space Physics (Cambridge: Cambridge Univ. Press), 166
Kulsrud, R. M. 2005, Plasma Physics for Astrophysics. Princeton Series in Astrophysics (Princeton, NJ: Princeton Univ. Press)
Lavine, E. S., & You, S. 2019, PhRvL, 123, 145002
Lebedev, S. V., Ciardi, A., Ampleford, D. J., et al. 2005, MNRAS, 361, 97
Lebedev, S. V., Frank, A., & Ryutov, D. D. 2019, RvMP, 91, 025002
Lewis, H. R., & Bellan, P. M. 1990, JMP, 31, 2592
Li, C. K., Tzeferacos, P., Lamb, D., et al. 2016, NatCo, 7, 13081
Li, Z.-Y. 1996, ApJ, 473, 873
Livio, M. 1999, PhR, 311, 225
Lynden-Bell, D. 2003, MNRAS, 341, 1360
Mestel, L. 1961, MNRAS, 122, 473
Nakamura, M., Garofalo, D., & Meier, D. L. 2010, ApJ, 721, 1783
Ouyed, R., & Pudritz, R. E. 1997, ApJ, 482, 712
Pudritz, R. E., Hardcastle, M. J., & Gabuzda, D. C. 2012, SSRv, 169, 27
Pudritz, R. E., & Ray, T. P. 2019, FrASS, 6, 54
Ryutov, D. D., Remington, B. A., Robey, H. F., & Drake, R. P. 2001, PhPl, 8, 1804
Salmeron, R., Königl, A., & Wardle, M. 2011, MNRAS, 412, 1162
Sauty, C. 1994, AnPh, 19, 459
Sauty, C., Meliani, Z., Lima, J. J. G., et al. 2011, A&A, 533, A46
Seo, B., & Bellan, P. M. 2018, PhPl, 25, 112703
Shibata, K., & Uchida, Y. 1986, SoPh, 103, 299
Stone, J. M., & Norman, M. L. 1992, ApJS, 80, 791
Tsinganos, K. 2007, Jets from Young Stars, 723 (Berlin: Springer), 117
Vlahakis, N., & Tsinganos, K. 1999, MNRAS, 307, 279
You, S., Yun, G. S., & Bellan, P. M. 2005, PhRvL, 95, 045002
Zhai, X., Li, H., Bellan, P. M., & Li, S. T. 2014, ApJ, 791, 40